Title

Photochemical Control of Exciton Superradiance in Light-Harvesting Nanotubes

Journal

ACS Nano, 12(5)

ISSN

1936-0851

Authors

Doria, Sandra
Sinclair, Timothy S
Klein, Nathan D
et al.

Publication Date

2018-05-22

DOI

10.1021/acsnano.8b00911

Peer reviewed

ACS NANO
Cite This: ACS Nano XXXX, XXX, XXX−XXX
www.acsnano.org

ARTICLE

Photochemical Control of Exciton Superradiance in Light-Harvesting Nanotubes

Sandra Doria,[†,‡,§] Timothy S. Sinclair,[†] Nathan D. Klein,[†] Doran I. G. Bennett,[∥] Chern Chuang,[†] Francesca S. Freyria,[†] Colby P. Steiner,[†] Paolo Foggi,[‡,⊥,#] Keith A. Nelson,[†] Jianshu Cao,[†] Alán Aspuru-Guzik,[∥] Seth Lloyd,[¶] Justin R. Caram,[*,†,□] and Moungi G. Bawendi[†]

[†]Department of Chemistry and [¶]Department of Mechanical Engineering, Massachusetts Institute of Technology, Cambridge, Massachusetts 02139, United States

[‡]European Laboratory for Non Linear Spectroscopy (LENS), Università degli Studi di Firenze, Via Nello Carrara 1, 50019 Sesto Fiorentino, Florence, Italy

[§]Dipartimento di Chimica "Ugo Schiff", Università degli Studi di Firenze, Via della Lastruccia, 3-13, 50019 Sesto Fiorentino, Florence, Italy

[∥]Department of Chemistry and Chemical Biology, Harvard University, 12 Oxford Street, Cambridge, Massachusetts 02138, United States

[⊥]INO−CNR, Istituto Nazionale di Ottica−Consiglio Nazionale delle Ricerche, Largo Fermi 6, 50125, Florence, Italy

[#]Dipartimento di Chimica, Biologia e Biotecnologie, Università di Perugia, Via Elce di Sotto 8, 06123, Perugia, Italy

[□]Department of Chemistry and Biochemistry, University of California, Los Angeles, Los Angeles, California 90095, United States

Supporting Information

ABSTRACT: **Photosynthetic antennae and organic electronic materials use topological, structural, and molecular control of delocalized excitons to enhance and direct energy transfer. Interactions between the transition dipoles of individual chromophore units allow for coherent delocalization across multiple molecular sites. This delocalization, for specific geometries, greatly enhances the transition dipole moment of the lowest energy excitonic state relative to the chromophore and increases its radiative rate, a phenomenon known as superradiance. In this study, we show that ordered, self-assembled light-harvesting nanotubes (LHNs) display excitation-induced photobrightening and photodarkening. These changes in quantum yield arise due to changes in energetic disorder, which in turn increases/decreases excitonic superradiance. Through a combination of experiment and modeling, we show that intense illumination induces different types of chemical change in LHNs that reproducibly alter absorption and fluorescence properties, indicating control over excitonic delocalization. We also show that changes in spectral width and shift can be sensitive measures of system dimensionality, illustrating the mixed 1−2D nature of LHN excitons. Our results demonstrate a path forward for mastery of energetic disorder in an excitonic antenna, with implications for fundamental studies of coherent energy transport.**

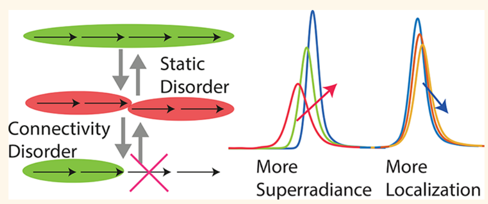

KEYWORDS: *excitons, superradiance, photobrightening, delocalization, coherence, light-harvesting nanotubes*

Excitation-induced changes in the fluorescent quantum yield are common features of solid-state optical materials. Photobrightening (PB) and photodarkening (PD) processes have been described for nanocrystal thin films (CdSe,[1,2] PbS,[3] CuBr,[4] Si[5]), organic−inorganic perovskites,[6] and conductive organic polymers (MEH-PPV,[7,8] P3HT[9]). While detailed mechanisms vary, most hypothesize that nonthermal charge-carrier trapping/detrapping processes underlie slow, seconds-long changes in film quantum yield due to the introduction of nonradiative decay channels.[10,11] We observe increasing and decreasing photoluminescence quantum yield of a highly coupled molecular aggregate arising due to changes in its *radiative rate*. We attribute these changes to increased/decreased excitonic superradiance manifesting through control of energetic disorder. Unraveling this unusual mechanism gives insight into the role microscopic energetic disorder plays in determining exciton delocalization and the emissive properties of molecular aggregates. Furthermore, this work shows that different forms of aggregate disorder can be induced using excitation light, providing a path forward to

Received: February 3, 2018
Accepted: April 27, 2018
Published: April 27, 2018

DOI: 10.1021/acsnano.8b00911
ACS Nano XXXX, XXX, XXX−XXX

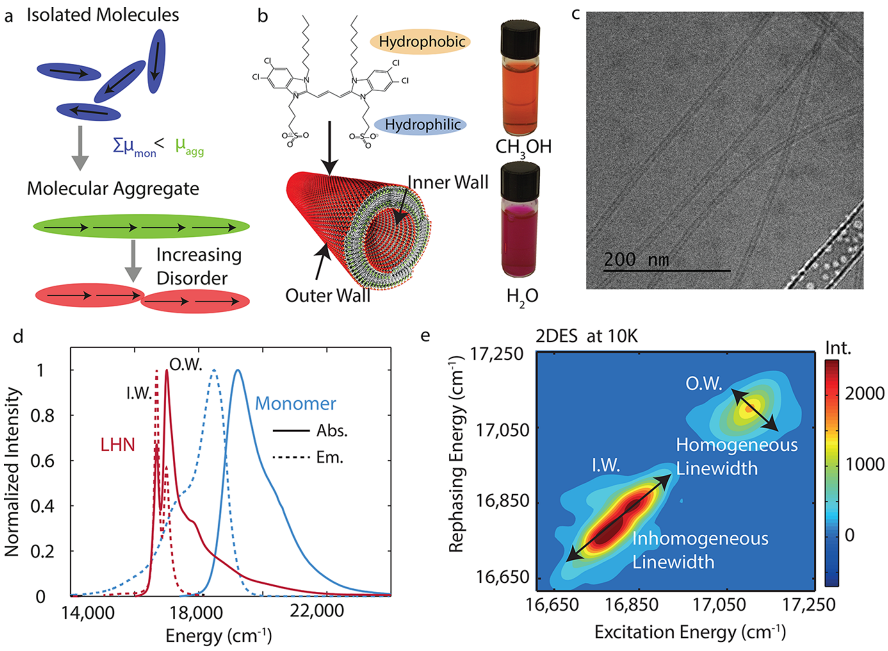

Figure 1. (a) Illustration of the delocalization of the exciton wave function from isolated molecules to a linear molecular aggregate. Upon aggregation, an extended transition dipole forms among coherent monomeric units, leading to an increase in the radiative rate due to larger collective dipoles. Energetic disorder decreases the excitonic spatial extent, as well as the transition dipole. (b) Chemical structure of the C8S3 monomer and 3D tubular structure of the LHNs (from Eisele *et al.*[24]). (c) Cryo-TEM of as-prepared LHN aggregates in sucrose–trehalose solution. (d) Absorption and emission of C8S3 monomers and LHNs. (e) Two-dimensional electronic spectra of LHNs at 10 K revealing the ensemble inhomogeneous line width of solid-state supported LHNs.

understanding and using disorder-modulated exciton transport in highly delocalized molecular aggregates.

In this article, we describe PB and PD processes in light-harvesting nanotubes (LHNs). LHNs are a model system for exploring coherent exciton dynamics owing to their highly delocalized excited states, strong dipole–dipole coupling, macroscopic uniformity, and large domain sizes.[12−17] We study LHNs in a sucrose/trehalose glass matrix, which greatly reduces photoinduced oxidative damage and maintains macroscopic order.[18] We find that intense resonant illumination sequentially photobrightens and reversibly photodarkens aggregate fluorescence. Using linear and time-resolved fluorescent spectroscopy and two-dimensional electronic spectroscopy, we probe LHN lifetimes and absorption/emission line shapes before, during, and following intense resonant excitation. We model these spectroscopic observables by introducing two different forms of energetic disorder in a model Hamiltonian: *site disorder* and *connectivity disorder.* Site disorder represents energetic variations of the site energies and/or couplings, while connectivity disorder arises from extreme local changes to a single site energy or its coupling to other sites, effectively scattering the exciton wave function. Through simple modeling, we show how disorder results in changes in exciton delocalization that, in turn, alter the absorption/emission peak position, line shape, and quantum yield by changing the degree of excitonic superradiance. Observation of the recovery of aggregate superradiance points to a photochemical mechanism for photoinduced changes in disorder.

RESULTS AND DISCUSSION

Energetic Disorder and Excitonic Superradiance. In Figure 1a, we present how energetic disorder modulates excitonic dynamics in a simplified linear chain aggregate. When monomer molecular transition dipoles are assembled end-to-end, their lowest energy excitonic state has a larger net transition dipole. If their transition dipole moments maintain a consistent phase relationship, these dipoles interact *coherently in phase* with an electromagnetic field leading to cooperative emission termed *excitonic superradiance.*[19] In the case of parallel collinear transition dipoles, the radiative rate $k_{r,e}$ for a one-dimensional J-aggregate is proportional to the effective number of coupled monomers participating in the coherent delocalization of the exciton according to eq 1.

$$k_{r,LHN} = Nk_{r,mon}\left(\frac{\lambda_{mon}}{\lambda_{LHN}}\right)^3 \tag{1}$$

Here, λ_{mon} and λ_{LHN} are the absorption maxima of exciton and monomer transition and $k_{r,mon}$ is the single monomer radiative rate.[20] Both static and dynamic energetic disorder decrease the coherent localization length of the exciton. Static disorder limits the coherence length by inducing buildup of random phase over N monomer units, limiting the extent of the aggregate delocalization. Dynamic disorder from environmental fluctuations further decoheres the wave function and leads to transient localization over a smaller number of sites. Therefore, static and dynamic disorder can act together to limit the size of the delocalized exciton and effect the radiative rate.

We use LHNs as a model system to explore extended excitonic states with superradiant emission.[21] In Figure 1b,c, we show the formation of these structures. LHNs self-assemble in water from the amphiphilic dye 3,3′-bis(2-sulfopropyl)-5,5′,6,6′-tetrachloro-1,1′-dioctylbenzimidacarbocyanine (C8S3) (Figure 1b). C8S3 forms tubular structures, which consist of two nested cylinders with diameters of 6 ± 1 and 13 ± 1 nm, respectively. We verify the formation of LHNs with

DOI: 10.1021/acsnano.8b00911
ACS Nano XXXX, XXX, XXX−XXX

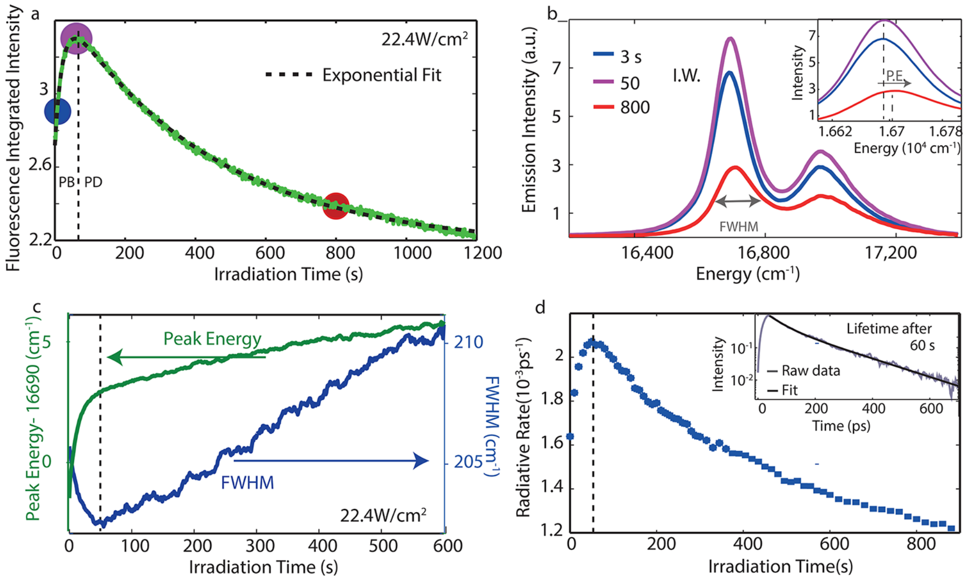

Figure 2. (a) Integrated fluorescence intensity of the LHNs in a solid matrix as a function of the irradiation time. The dotted line shows a biexponential fit (eq 3). (b) Three fluorescence spectra collected after 3, 50, and 800 s of irradiation (corresponding to the circles in a). Inset shows the blue-shift of the inner wall emissive band during irradiation. (c) fwhm (blue) and peak energy (green) as a function of irradiation time. The band narrows during photobrightening and broadens during photodarkening, while continuously blue-shifting during PB and PD. (d) Radiative rate from eq 2, increasing during photobrightening and decreasing during photodarkening. Inset shows raw streak camera data fit using a single exponential.

cryo-TEM (Figure 1c). In Figure 1d, we show that LHN formation leads to a 2250 cm^{-1} red-shift of the absorption spectrum (from 19 250 to 17 000 cm^{-1}) and the appearance of multiple narrow features. The observed red-shift is the result of changes in the local environment, dipole solvation, and (primarily) significant negative coupling between monomer units, although the precise contribution of each parameter is highly dependent on details of the structural arrangement.[12,22−24] Complementary absorption and linear dichroism spectroscopy of LHNs show that eight features underlie the absorption spectrum. This suggests that chromophores arrange in a two-molecule unit cell, leading to four electronic transitions for each wall, with two parallel and two perpendicular relative to the long axis of the linear aggregate.[25] This study focuses on the lowest energy band, representing the dominant parallel transition of the inner wall, from which most of the emission occurs, although some arises from the thermally occupied parallel transition of the outer wall at 16 690 cm^{-1}.[26]

In coupled aggregates, energetic disorder in each monomer unit leads to motional/exchange narrowing of the line width for the extended delocalized state.[27] In Figure 1e we show two-dimensional electronic spectroscopy (2DES) on LHNs at 10 K, which we use to experimentally characterize the inner wall line width and to study how photoinduced disorder changes aggregate line shapes. Briefly, 2DES separates static inhomogeneous disorder along the diagonal and “dynamic” homogeneous disorder on the antidiagonal line shape.[14,28] 2DES correlates the initial energy of absorption of light to the subsequent response of the system to photoexcitation. At zero population time, 2DES allows us to estimate the inhomogeneous line shape prior to homogeneous sources of environmental dephasing and intrinsic exciton relaxation. 2DES spectra at 10 K were measured to determine the aggregate *inhomogeneous* absorptive line width, which will be used to model the effect of disordered LHN photophysics.

Excitation-Induced Photobrightening and Photodarkening. We describe the effect of high-power photoexcitation on matrix-stabilized LHNs in Figure 2. In Figure 2a we plot the integrated fluorescence under continuous illumination with a laser centered at 532 nm (22.3 W/cm^2). We observe an initial increase of fluorescent quantum yield (photobrightening), followed by a decrease in quantum yield (photodarkening), on longer time scales. This behavior is highly reproducible (Figure 3a and Figure S1) under both pulsed and CW excitation, and at different wavelengths of excitation (400 and 532 nm). We plot three sample fluorescent spectra for different irradiation times in Figure 2b. We display two spectra during PB (after 3 and 50 s) and the third during PD (800 s). We observe fluorescent spectral narrowing during PB and broadening during PD. Fitting to a pseudo-Voigt profile as described in the Supporting Information (eq S1), in Figure 2c we plot the peak position (a_1) and fwhm (1.6371 a_2) of the inner wall fluorescence feature derived from the modified Whiting approximation.[29] These two parameters show narrowing and rapid blue-shift of the inner wall emission during PB, followed by broadening and sustained blue-shift during PD.

In Figure 2d we plot the measured radiative rate during PB and PD. We irradiate the sample with 22 W/cm^2 at 532 nm to induce the change in quantum yield (QY) and periodically record fluorescent lifetime data on a streak camera using a lower power 0.2 W/cm^2 ultrafast excitation at 400 nm, in order not to perturb the conditions established by the high-power resonant excitation (shown in Figure S2). The recorded lifetime data after 60 s of irradiation are shown in the inset of Figure 2d, which we fit to a single exponential decay, $a_0 \exp(-k_{tot}t)$. The recorded total rate k_{tot} is shown in Figure S2b. We calculate the radiative rate as

$$k_r(t) = k_{tot}(t)\,\mathrm{QY}(t) = k_{tot}(t)\frac{\mathrm{QY}(0)}{I(0)}I(t) \qquad (2)$$

DOI: 10.1021/acsnano.8b00911
ACS Nano XXXX, XXX, XXX−XXX

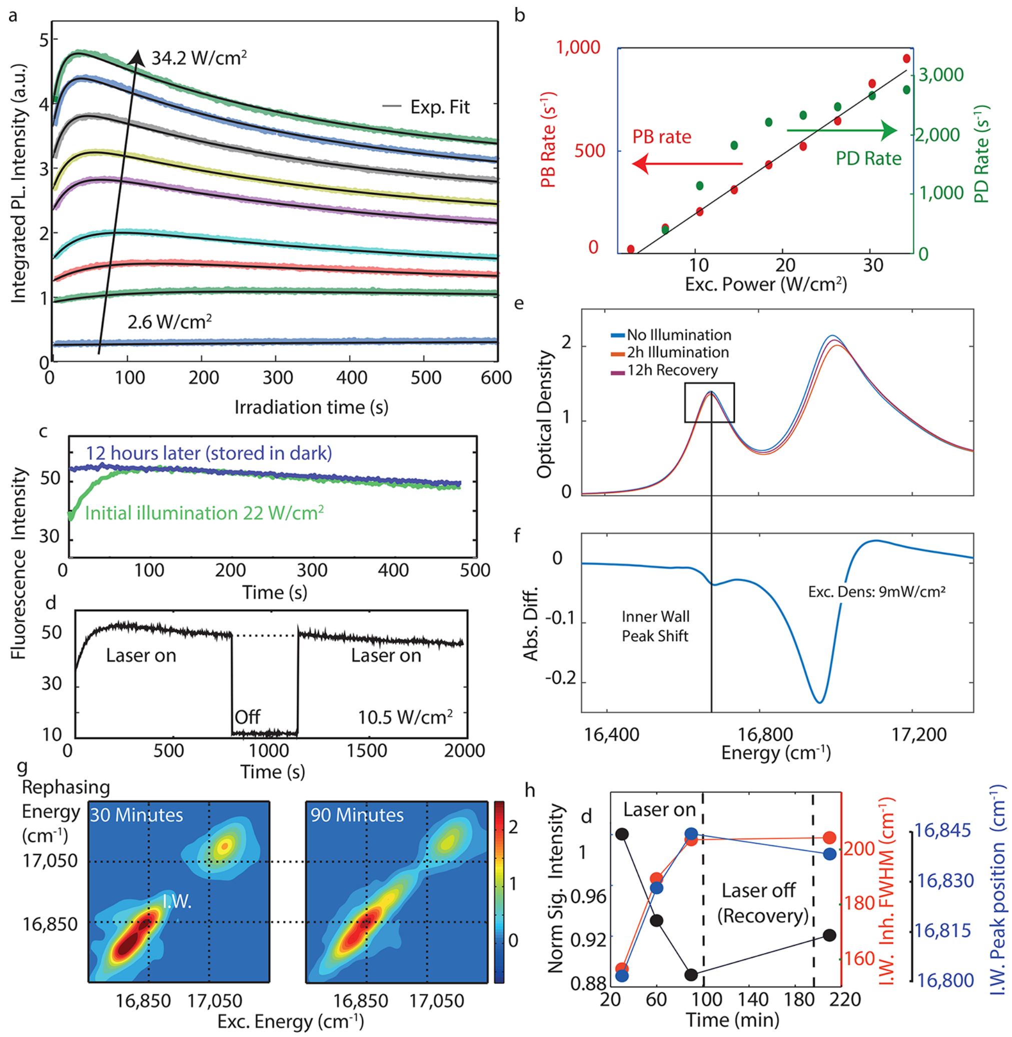

Figure 3. (a) Integrated fluorescence intensity of the LHNs in a sugar matrix as a function of the irradiation time (excitation at 532 nm) and illumination per unit area. (b) Rates of PB and PD, as a function of incident intensity (c) Fluorescence intensity recorded during illumination of the sample (green) and 12 h later (blue curve). We observe near complete recovery of the fully photobrightened signal, following PD. (d) Fluorescence intensity during illumination showing partial recovery of the signal after the excitation is turned off for 5 min. (e) Absorption spectra of the sample taken under weak LED illumination after 2 and 12 h in the dark (showing partial recovery). (f) Difference spectra between initial and after 2 h of illumination showing a slight blue-shift, consistent with photodarkening behavior. (g) 2DES taken after 30 and 90 min of irradiation showing a shift and decrease in peak intensity. (h) Analysis of the rephasing signal from the 2DES spectra (Figure S3) recorded at different irradiation times and after the illumination was turned off for 90 min. We plot the signal intensity (left axis) of the inner wall peak position and inner wall fwhm (right axis).

where QY(t) is extracted from the integrated fluorescence ($I(t)$) as a function of illumination rescaled by QY(0) measured under low flux in an integrating sphere (Supporting Information for details). We observe an increase of the total rate k_{tot} and the radiative rate during PB, followed by a decrease during PD. These trends are reproduced with higher power excitation at 400 nm, consistent with the lower absorption of LHNs in that spectral region.

In Figure 3a we show PB and PD behavior as a function of excitation power. We fit total fluorescent intensity to the sum of an exponential rise and an exponential decay to describe PB and PD, respectively:

$$I(t) = a_0(1 - e^{-k_1 t}) + a_1 e^{-k_2 t} \tag{3}$$

We plot the rates $k_{1,2}$ in Figure 3b. Within the analyzed range of excitation power, the PB rate scales linearly with the illumination power per unit area, while the PD rate shows nonlinearity at higher flux.

In Figure 3c–f we examine the photodarkening behavior in more detail. In Figure 3c we demonstrate that the photodarkened state slowly recovers with no excitation. We see recovery after 12 h (Figure 3c), and partial recovery in 5 min (Figure 3d). Photodarkening behavior also manifests in the collected 2DES signal shown in Figure 3e and SI Figure S3. We observe similar behavior to that shown for fluorescence in Figure 3. Decreased signal accompanies a shift in the peak location and peak fwhm (Figure 3f). A partial recovery in all parameters also occurs after 90 min in the dark. Interestingly the recovery happens both at room temperature (Figure 3c,d) and at 10 K (Figure 3e,f), suggesting weak temperature dependence.

The observed photobrightening and photodarkening behavior is distinct from temperature-induced changes in aggregate spectra. As we show in Figure S6 and in a prior publication,[18] increasing temperature results in decreased intensity, broadening of spectral features, and a distinct *red-shift*, while

DOI: 10.1021/acsnano.8b00911
ACS Nano XXXX, XXX, XXX−XXX

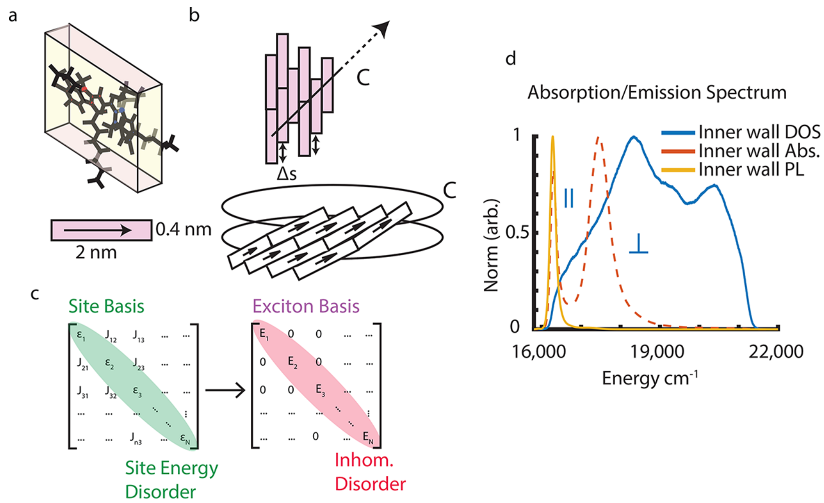

Figure 4. (a) C8S3 molecule within the brick used. (b) Bricks are placed in a 2D grid with set slip Δs, then wrapped according to chiral vector C, which leads to helical aggregates. (c) From this geometry, off-diagonal elements are calculated and the corresponding system Hamiltonian is diagonalized to find the density of states. (d) We plot the density of states and the absorption and room-temperature emission for the inner wall of the LHN.

photodarkening results in a *blue-shift*. Coupling this observation with the observation of very slow recovery dynamics leads us to conclude that a distinct, non-temperature-related effect is responsible for the observed photodarkening.

Modeling Static Disorder in LHNs. We apply a "rolled-brick" model of LHN morphology to understand how line shapes and radiative rates change in response to a change in *site* static disorder. Using the inner wall radius from TEM and the assumption of closely packed molecules with helical symmetry, we build a simple model of the inner wall LHN absorption and emission following prior methods.[22,30] C8S3 "bricks" with $x-y$ projection 2×0.4 nm (Figure 4a) are tiled in a 2D brick layer structure with a slip of 0.75 nm between successive layers of bricks. This enforces net negative coupling, and thus an overall red-shift of the absorption peak and J-aggregation. We then wrap the structure along a chiral vector with length set by the circumference of the LHN shown in Figure 4b. The wrapping leads to splitting and redistribution of the absorption cross-section of parallel- and perpendicular-polarized transitions of the LHN. To determine the coupling energy between aggregates, the geometry of a C8S3 molecule, modified to fit the PM6 basis set and optimized with a PM6 Hamiltonian,[31] is implemented in Gaussian09[32] in the gas phase (see SI and Figure S7 for details). Transition density charges are extracted from standard ZINDO/S calculations based on this optimized geometry.[33] Couplings between monomers are calculated using these transition density charges.

The site-basis Hamiltonian shown in Figure 4c is

$$H = \sum_{n \neq m} J(n, m) a_n^{\dagger} a_m + \sum_n \epsilon_n a_n^{\dagger} a_n \tag{4}$$

where $J(n, m)$ is the coupling between the excited states in site n and m, $a_n^{\dagger}$ is the raising operator for site n, and ϵ_n is a Gaussian random variable with mean ϵ_0, the excitation frequency of an individual C8S3 molecule, and standard deviation σ. To determine the excitonic properties, we diagonalize the matrix. The corresponding excitonic wave functions are $\phi_n = \sum_m q_{mn} \epsilon_n$, with energies d_n and corresponding overall transition dipole $\mu_n = \mu_{\mathrm{mon}} \sum_m q_{mn} \hat{\mu}_m$ where $\hat{\mu}_m$ is the unit vector parallel to the transition dipole of molecule m.

Figure 4d shows the density of states calculated: $\mathrm{DOS}(\omega) = \sum_n \delta(\omega - d_n)$. The inhomogeneous (zero-temperature) absorption spectrum is a dipole-weighted DOS, while the emission spectrum is further weighted with a Boltzmann distribution, *e.g.*,

$$\mathrm{PL}(\omega) = \sum_n |\mu_n|^2 \delta(\omega - d_n) \frac{1}{Z_n} \mathrm{e}^{-\beta d_n} \sqrt{b^2 - 4ac}$$

with $Z_n = \sum_n \mathrm{e}^{-\beta d_n}$. This approach allows us to find the amount of site disorder that agrees with the inhomogeneous line shape due to static disorder. We find that $\sigma = 582$ cm^{-1} for the distribution of excitation frequencies, which gives good agreement with a 150 cm^{-1} fwhm measured using 2DES at 10 K and low-temperature absorption spectra of the parallel inner wall feature (Figure S8).

We use this model as a minimal basis to explore the effect of different forms of static disorder on spectral observables. We note more sophisticated models have been developed to explain observed splittings in parallel and perpendicular spectra.[23,24] Furthermore, recent work has highlighted the possible importance of charge transfer (CT) coupling on coupling between nearest neighbors in perylene tetracarboxydiimide (PDI)-based materials and conductive polymer systems.[34] To date, no work has been done to calculate the magnitude of CT couplings for cyanine dye aggregates, although it may provide additional insight into the observed spectral features.

Modeling Photobrightening and Photodarkening. In Figure 5 we simulated the inner wall emission spectrum varying the underlying Hamiltonian to include the effects of photo-induced changes in disorder. In Figure 5a we plot the emission spectra for three different Gaussian distributions of site disorder. We observe an increase in the intensity (Figure 5c), a decrease in the fwhm, and a blue-shift in the peak emission energy in Figure 5d, matching the experimental results presented in Figure 3c. We conclude that PB occurs due to light-induced *annealing* of the aggregate, which increases the exciton delocalization by reducing disorder in the molecular lattice. Our results suggest that starting from an initial site disorder of 500 cm^{-1}, we observe a ~50 cm^{-1} decrease in the

DOI: 10.1021/acsnano.8b00911
ACS Nano XXXX, XXX, XXX−XXX

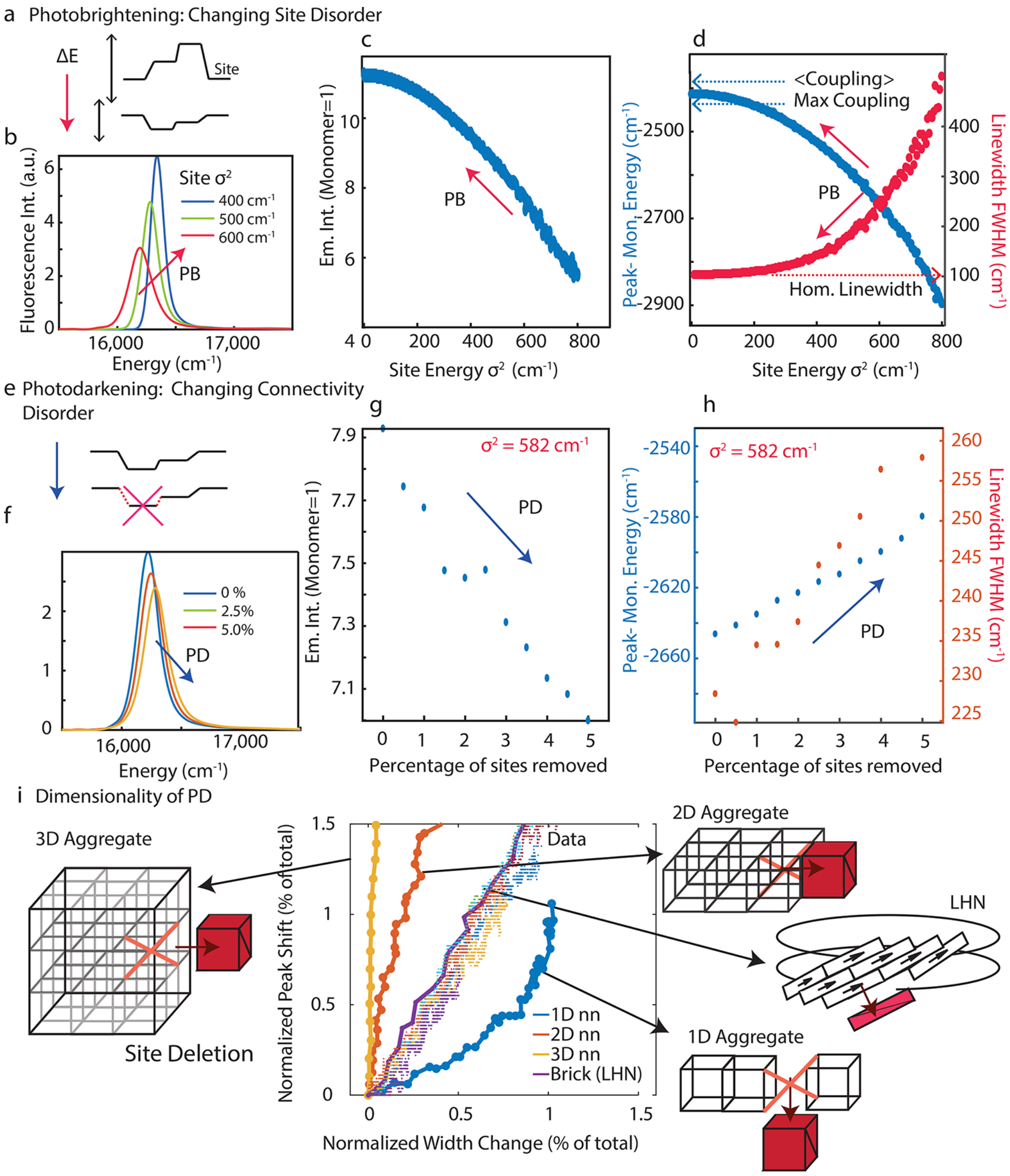

Figure 5. (a) Changing the site disorder in the Hamiltonian results in a change in the emission spectra plotted in (b). The emission intensity (c) and peak shift and fwhm (d) for varying amounts of diagonal (static) disorder. In (e) we remove sites and zero out their coupling to model connectivity disorder and plot the emission spectrum in (f). Intensity (g) and peak shift and fwhm changes (h) are consistent with observed trends during photodarkening. (i) We plot the change in peak width *vs* peak shift, both normalized by the absolute peak shift with respect to monomer energy and compare to Monte Carlo simulations of idealized aggregates with one-, two-, and three-dimensional connectivity. We also model the rolled-brick aggregate. The data (dotted lines) agree with the LHN model and suggest that the aggregate lies somewhere between one- and two-dimensional connectivity.

standard deviation in site energies. This small change in static disorder can increase the observed quantum yield by nearly 30%, matching our experimental results.

During PD, we observed a reversal of all trends *except* the blue-shift of the peak position. PD is modeled in Figure 5e−h by "removing" individual monomers from the aggregate structure for 582 cm^{-1} of static disorder (introducing connectivity disorder). We plot the emission spectra in Figure 5f with different concentrations of "turned off" monomers within an aggregate. This process leads to a decrease in PL intensity (Figure 5g) accompanied by an increase in the fwhm and peak energy (Figure 5h). Our results suggest that site deletion is a possible mechanism for photodarkening, leading to emission peak shift and fwhm increase.

In Figure 5i we explore the photodarkening behavior more fully. Here we show the scatter plot of changes in line width *versus* changes in peak location of the inner wall emission in the PD region. Since this type of plot reveals the connectivity and the dimensionality of the system, we also present the numerical results of idealized, nearest-neighbor-coupled cubic lattices of different dimensions. Note that both quantities have been normalized by the total amount of peak shift compared to monomers. Given the small amount of site deleted, excitons in higher dimensional aggregates are rather robust against site deletion, where the 1D the connectivity between adjacent segments is completely destroyed by the deletion of even a single site. This justifies the treatment of the site deletion effect perturbatively, where the peak shift and width are given by[35,36]

DOI: 10.1021/acsnano.8b00911
ACS Nano XXXX, XXX, XXX−XXX

$$\text{shift}(\sigma) = \langle k = 0|V|k = 0\rangle = 2d\sigma \tag{5}$$

$$\text{width}(\sigma) = \pi \sum_{j\neq 0} |\langle j|V|k = 0\rangle|^2 \delta(E_j - E_0) = \pi\sigma^2\rho_0(E_0) \tag{6}$$

where σ is the ratio of the sites deleted, $|k\rangle$ is the Bloch wave function with quasi-momentum k and energy E_k, V represents the excitonic interactions removed, $d = 1-3$ is the dimensionality, and $\rho_0(E)$ is the density of states. Both of these are given in units of the excitonic coupling. We note that the prefactor in eq 5 is essentially the sum of couplings of a representative site, so the direction of the shift would be opposite in an H-aggregate. The shift, given by the first-order perturbation result, is a bilinear function of d and σ. On the contrary the width, given by the Golden Rule, is much more sensitive to the dimensionality.[17,37] This explains that the higher the dimension, the steeper curve one observes as seen in the figure. On the other hand, the experimental data lie in between the results of 1D and 2D models, close to that of a more realistic rolled-brick model.

The implication of such agreement is 2-fold. First, this confirms that the excitons in LHN are fully delocalized over the circumference so that the LHN can be regarded as a quasi-1D construct. As a consequence, the transport of excitons within enjoys both the directionality of 1D systems and the robustness against environmental disorder and noise as in 2D systems.[17,18] Second, this demonstrates light-induced PD as a useful and sensitive probe to the dimensionality of similar excitonic systems. A detailed examination of disorder-induced spectral changes and their relation to dimensionality will be included in a forthcoming report. We note that the observed trends shown in Figure 5i are internally calibrated and depend only on the overall dimensionality and sign of the coupling rather than details of the coupling calculation itself. This suggests that our analysis is consistent regardless of more detailed (and accurate) models of aggregate photophysics.

The two forms of disorder needed to reproduce the spectral results point to possible chemical mechanisms for photobrightening/darkening. During excitation, the variance in site energies decreases following first-order kinetics, suggesting a limited rearrangement of the aggregate structure that increases its overall site-energy order. The rate of PB varies linearly with the absorption of the aggregate and the photon flux, which suggests that nonradiative recombination (local heating) leads to the observed reorganization of the aggregate structure. This behavior is distinct by changing the temperature of the aggregate matrix, suggesting an irreversible annealing process. After the aggregate fully anneals, we begin to observe PD, with decreased PL intensity, increased line width, and *continued peak blue-shift*. PD appears to be fully reversible over hour-long time scales at both room temperature and 5 K. We model this through the introduction of defect sites that do not participate in the exciton delocalization. Exciton lifetime increases during PD, suggesting that these defect *do not act as nonradiative trap states*. These states instead scatter the delocalized wave function and decrease the amount of excitonic superradiance. We speculate a possible mechanism could be photoinduced charging of the aggregate, which has been invoked in prior experiments to explain long-lived reversible photodarkened states.[10] Supporting this, saturation behavior in the rate of photodarkening observed in Figure 3b is consistent with nongeminate charge recombination at high fluxes. Exploring the source of connectivity disorder will be the subject of future work.

CONCLUSION

LHNs have highly coherent excitons, with delocalization that extends over 10's of monomer units.[21] Additionally, LHNs show long-range exciton motion, partially mediated by coherent dynamics.[18,38] However, controllably modulating disorder to test the role of delocalization and the resulting coherence on energy transfer remains a significant challenge. Intense illumination leads to photobrightening and photodarkening in LHNs. For photobrightening we find an increase in aggregate quantum yield connected to a peak blue-shift, a decrease in fwhm, and an increase in the total emissive rate. Modeling this behavior suggests emission is mediated by a change in the extent of the average exciton *coherence domain*, leading to changes in excitonic superradiance. Our results demonstrate that the quantum yield can increase by up to 30% with a small change in the overall static disorder.

During photodarkening we observe a decrease in quantum yield accompanied by an increased fwhm, a peak blue-shift, and a decreased emission rate. Interestingly, PD is reversible in the dark. This suggests a different form of disorder modulation that decreases the overall delocalization without changing the overall static disorder. We model PD by removing individual monomers from the excitonic density of states, which may reflect isomerization, individual site charging, or long-lived triplet formation. We speculate that the formation of charged monomer units can lead to the slow yet reversible PD observed. This form of PD is a sensitive independent metric of the dimensionality of the aggregate system and points to how a quasi one-dimensional system can be robust to common forms of disordering.

Illumination allows us to anneal aggregates *and* selectively introduce defect states, providing a quantitative method to explore the role of delocalization on excitonic superradiance. The sensitivity of quantum yield and thus excitonic superradiance to parameters may explain large variance in estimated excitonic diffusion length in the literature (ranging from <50 nm to 1.7 μm).[18,24,38] The use of photoinduced modulation can enable researchers to carefully engineer disorder and study its effect on exciton motion. As energetic disorder dephases coherent excitons, modulating it provides a path forward to understanding quantum mechanical phase in exciton transport in an exciting functional antenna material.

EXPERIMENTAL METHODS

Sample Preparation. Light-harvesting nanotubes self-assemble from amphiphilic C8S3 dye molecules (FEW Chemicals). We prepared a stock solution of 2.9×10^{-3} M C8S3 in methanol (99.9% GC, Sigma-Aldrich). We mixed 260 μL of stock solution with 1 mL of deionized water. LHNs were stored in the dark over 24 h to aggregate and stabilize. To prevent oxidative photobleaching, the aqueous LHN solution was mixed at 50/50 v/v ratio with a saturated solution of 50% by weight mixture of sucrose and trehalose (Sigma-Aldrich). Then 100 μL of the final solution was spread on a 0.2 mm path length cuvette (Starna cells), in order to obtain a thick film. The sample was stored under vacuum (0.5 atm) for 24 h. LHNs were thusly embedded in a photostable amorphous dry glass sugar matrix.

Photobrightening and Photodarkening. Fluorescence intensity measurements of LHNs in a sugar matrix were collected using a homemade fluorimeter (Figure S4). The sample was placed under vacuum in an ST-100 (Janis) coldfinger cryostat to prevent photo-oxidation. We used four laser systems to assess spectral dynamics as a

DOI: 10.1021/acsnano.8b00911
ACS Nano XXXX, XXX, XXX−XXX

function of incident power: (1) a supercontinuum pulsed ultrafast laser, the Koheras SuperK Extreme (NKT Photonics, 78 MHz repetition rate, spectral dual filter output) set to 532 nm; (2) continuous wave excitation (Thorlabs laser diode CPS532) at 532 nm; (3) 400 nm pulsed excitation, frequency doubled from a femtosecond Ti:S oscillator, Coherent MIRA; and (4) a Melles Griot diode laser at 400 nm. For the results plotted in Figure 2a, we varied the excitation power from to 2.6 to 34.2 W cm^{-2} of the SuperK. The excitation beam was focused on the sample by an 8 in. lens (25 μm Gaussian focus diameter measured using a razor blade). We collected the epifluorescence signal using a 2 in. parabolic silver mirror, which was directed into an Ocean Optics HR2000 visible spectrometer. Identical results were collected for both pulsed and CW laser sources, although the required powers were significantly higher (on the order of 500 W/cm^2) for 400 nm excitation, consistent with direct absorption of the molecular aggregate. Figure S2 shows the results obtained in the case of CW excitation at 532 nm.

Emission from the above experiment was also directed into a Hamamatsu C5680 streak camera in order to collect fluorescence lifetime during irradiation. Here the femtosecond output of a Ti:S oscillator (Coherent MIRA 800 nm output, 78 MHz repetition rate, Coherent Verdi G series 532 nm pump) was doubled to excite the LHNs at 400 nm. The streak camera was set to syncroscan mode (using the syncroscan sweep unit M5675) with a temporal resolution of 14 ps. We induced PB and PD using the SuperK laser exciting at 532 nm (22.3 W cm^{-2}), blocking the beam every 10 s, to collect the lifetime. Lifetime data were recorded at significantly lower fluxes (0.2 W cm^{-2}), previously found to induce no changes in the overall fluorescent spectrum.

Absorption measurements of illumination-induced changes in LHNs in a sugar matrix were collected using a Cary 5000 spectrophotometer (Agilent). The sample was illuminated using a 530 nm M530L3 LED (Thorlabs) positioned against the cryostat window. The resulting illumination was measured to be 9 mW/cm^2 across the sample area. Spectra were collected following every 10 min of illumination. To collect the absorption spectrum, the LED was turned off for a total of 2 min as the spectrophotometer scanned and then turned back on. The experiment was carried out until a total illumination time of 120 min was reached, after which the sample was left under vacuum in the dark to recover. Following 12 h of recovery, the absorption spectrum was collected again.

Two-Dimensional Electronic Spectroscopy. 2DES spectra were collected as described in prior publications.[39] A noncollinear optical parametric amplifier was pumped by a Coherent Libra Ti:sapphire regenerative amplifier laser system with 100 fs, 800 nm pulses at 10 kHz. The NOPA spectrum was centered at 17 260 cm^{-1} with a full width at half-maximum of 1100 cm^{-1}. The laser was focused onto a transmissive diffractive optic to generate four beams in the BOXCARS geometry. The four beams were then relay imaged by common path optics into a pulse shaper comprising a ruled reflectance grating, achromatic cylindrical lens, and 2D spatial light modulator (SLM). In the pulse shaper, each beam is spectrally dispersed onto vertically distinct regions of the 2D SLM for independent temporal shaping. After temporal shaping, the four beams exit the pulse shaper and are relay imaged to sample position. Ultrafast laser pulses were compressed to 35 fs with an average pulse energy of 45 pJ. The beams were focused to approximately 30 μm for a fluence of about 6(0.4) μJ/cm^2. For each 2D spectrum, the coherence time delay between pulses 1 and 2 was scanned from 0 to 720 fs in 5 fs steps. The signal was measured using eight-step phase cycling and spectral interferometry to recover the full electric field. Figure S5 shows the beams' spectra on top of the sample absorption spectrum.

ASSOCIATED CONTENT

Supporting Information

The Supporting Information is available free of charge on the ACS Publications website at DOI: 10.1021/acsnano.8b00911.

Repeat measurments, 2D electronic spectra, fitting strategy, and experimental setup; further details on the calculation of couplings, modeling of absorption spectra, and role of disorder in exciton delocalization (PDF)

AUTHOR INFORMATION

Corresponding Author

*E-mail: jcaram@chem.ucla.edu.

ORCID

Sandra Doria: 0000-0002-9440-1643
Doran I. G. Bennett: 0000-0001-8322-7371
Francesca S. Freyria: 0000-0002-2710-5545
Alán Aspuru-Guzik: 0000-0002-8277-4434
Justin R. Caram: 0000-0001-5126-3829
Moungi G. Bawendi: 0000-0003-2220-4365

Notes

The authors declare no competing financial interest.

ACKNOWLEDGMENTS

J.R.C. and T.S. were funded by the Department of Energy (DOE) through the DOE Center for Excitonics (an Energy Frontiers Research Center funded by the U.S. DOE, Office of Science, Office of Basic Energy Sciences, through grant no. DE-527 SC0001088). F.S.F. was supported by Eni SpA under the Eni- MIT Alliance Solar Frontiers Center. N.D.K. was funded by the DOE Office of Science, Basic Energy Sciences through grant no. DE-FG02-07ER46454. S.D., T.S.S., N.D.K., F.S.F, C.P.S., and J.R.C. performed the experiments. T.S.S., D.I.G.B., C.C., performed simulations. All authors contributed to data interpretation and writing the manuscript. We would also like to acknowledge the reviewers for helpful feedback and ideas for additional experiments.

REFERENCES

(1) Tice, D. B.; Frederick, M. T.; Chang, R. P. H.; Weiss, E. A. Electron Migration Limits the Rate of Photobrightening in Thin Films of CdSe Quantum Dots in a Dry N2 (G) Atmosphere. *J. Phys. Chem. C* **2011**, *115*, 3654−3662.

(2) Asami, H.; Abe, Y.; Ohtsu, T.; Kamiya, I.; Hara, M. Surface State Analysis of Photobrightening in CdSe Nanocrystal Thin Films. *J. Phys. Chem. B* **2003**, *107*, 12566−12568.

(3) Peterson, J. J.; Krauss, T. D. Photobrightening and Photodarkening in PbS Quantum Dots. *Phys. Chem. Chem. Phys.* **2006**, *8*, 3851−3856.

(4) Oda, M.; Shen, M. Y.; Saito, M.; Goto, T. Photobrightening of CuBr Nanocrystals in PMMA. *J. Lumin.* **2000**, *87−89*, 469−471.

(5) Miller, J. B.; Van Sickle, A. R.; Anthony, R. J.; Kroll, D. M.; Kortshagen, U. R.; Hobbie, E. K. Ensemble Brightening and Enhanced Quantum Yield in Size-Purified Silicon Nanocrystals. *ACS Nano* **2012**, *6*, 7389−7396.

(6) deQuilettes, D. W.; Zhang, W.; Burlakov, V. M.; Graham, D. J.; Leijtens, T.; Osherov, A.; Bulović, V.; Snaith, H. J.; Ginger, D. S.; Stranks, S. D. Photo-Induced Halide Redistribution in Organic−inorganic Perovskite Films. *Nat. Commun.* **2016**, *7*, 11683.

(7) Szymanski, C.; Wu, C.; Hooper, J.; Salazar, M. A.; Perdomo, A.; Dukes, A.; McNeill, J. Single Molecule Nanoparticles of the Conjugated Polymer MEH−PPV, Preparation and Characterization by Near-Field Scanning Optical Microscopy. *J. Phys. Chem. B* **2005**, *109*, 8543−8546.

(8) Yu, Z.; Barbara, P. F. Low-Temperature Single-Molecule Spectroscopy of MEH-PPV Conjugated Polymer Molecules. *J. Phys. Chem. B* **2004**, *108*, 11321−11326.

(9) Thiessen, A.; Vogelsang, J.; Adachi, T.; Steiner, F.; Vanden Bout, D.; Lupton, J. M. Unraveling the Chromophoric Disorder of poly(3-Hexylthiophene). *Proc. Natl. Acad. Sci. U. S. A.* **2013**, *110*, E3550−E3556.

(10) Jensen, R. A.; Coropceanu, I.; Chen, Y.; Bawendi, M. G. Thermal Recovery of Colloidal Quantum Dot Ensembles Following Photoinduced Dimming. *J. Phys. Chem. Lett.* **2015**, *6*, 2933−2937.

(11) Dong, L.; Archambault, J. L.; Reekie, L.; Russell, P. S. J.; Payne, D. N. Photoinduced Absorption Change in Germanosilicate Preforms: Evidence for the Color-Center Model of Photosensitivity. *Appl. Opt.* **1995**, *34*, 3436−3440.

(12) Knoester, J. Optical Properties of Helical Cylindrical Molecular Aggregates: The Homogeneous Limit. *J. Phys. Chem. B* **2002**, *106*, 149−186.

(13) Eisele, D. M.; Cone, C. W.; Bloemsma, E. A.; Vlaming, S. M.; van der Kwaak, C. G. F.; Silbey, R. J.; Bawendi, M. G.; Knoester, J.; Rabe, J. P.; Vanden Bout, D. A. Utilizing Redox-Chemistry to Elucidate the Nature of Exciton Transitions in Supramolecular Dye Nanotubes. *Nat. Chem.* **2012**, *4*, 655−662.

(14) Yuen-Zhou, J.; Arias, D. H.; Eisele, D. M.; Steiner, C. P.; Krich, J. J.; Bawendi, M. G.; Nelson, K. A.; Aspuru-Guzik, A. Coherent Exciton Dynamics in Supramolecular Light-Harvesting Nanotubes Revealed by Ultrafast Quantum Process Tomography. *ACS Nano* **2014**, *8*, 5527−5534.

(15) Clark, K. A.; Krueger, E. L.; Vanden Bout, D. A. Direct Measurement of Energy Migration in Supramolecular Carbocyanine Dye Nanotubes. *J. Phys. Chem. Lett.* **2014**, *5*, 2274−2282.

(16) Haverkort, F.; Stradomska, A.; de Vries, A. H.; Knoester, J. Investigating the Structure of Aggregates of an Amphiphilic Cyanine Dye with Molecular Dynamics Simulations. *J. Phys. Chem. B* **2013**, *117*, 5857−5867.

(17) Chuang, C.; Lee, C. K.; Moix, J. M.; Knoester, J.; Cao, J. Quantum Diffusion on Molecular Tubes: Universal Scaling of the 1D to 2D Transition. *Phys. Rev. Lett.* **2016**, *116*, 196803.

(18) Caram, J. R.; Doria, S.; Eisele, D. M.; Freyria, F. S.; Sinclair, T. S.; Rebentrost, P.; Lloyd, S.; Bawendi, M. G. Room-Temperature Micron-Scale Exciton Migration in a Stabilized Emissive Molecular Aggregate. *Nano Lett.* **2016**, *16*, 6808−6815.

(19) Mcrae, E. G.; Kasha, M. Enhancement of Phosphorescence Ability upon Aggregation of Dye Molecules. *J. Chem. Phys.* **1958**, *721*, 7−9.

(20) Kamalov, V. F.; Struganova, I. a.; Yoshihara, K. Temperature Dependent Radiative Lifetime of J-Aggregates. *J. Phys. Chem.* **1996**, *100*, 8640−8644.

(21) Eisele, D. M.; Knoester, J.; Kirstein, S.; Rabe, J. P.; Vanden Bout, D. A. Uniform Exciton Fluorescence from Individual Molecular Nanotubes Immobilized on Solid Substrates. *Nat. Nanotechnol.* **2009**, *4*, 658−663.

(22) Didraga, C.; Pugžlys, A.; Hania, P. R.; von Berlepsch, H.; Duppen, K.; Knoester, J. Structure, Spectroscopy, and Microscopic Model of Tubular Carbocyanine Dye Aggregates. *J. Phys. Chem. B* **2004**, *108*, 14976−14985.

(23) Megow, J.; Röhr, M. I. S.; am Busch, M. S.; Renger, T.; Mitrić, R.; Kirstein, S.; Rabe, J. P.; May, V. Site-Dependence of van Der Waals Interaction Explains Exciton Spectra of Double-Walled Tubular J-Aggregates. *Phys. Chem. Chem. Phys.* **2015**, *17*, 6741−6747.

(24) Eisele, D. M.; Cone, C. W.; Bloemsma, E. A.; Vlaming, S. M.; van der Kwaak, C. G. F.; Silbey, R. J.; Bawendi, M. G.; Knoester, J.; Rabe, J. P.; Vanden Bout, D. A. Utilizing Redox-Chemistry to Elucidate the Nature of Exciton Transitions in Supramolecular Dye Nanotubes. *Nat. Chem.* **2012**, *4*, 655−662.

(25) Eisele, D. M.; Arias, D. H.; Fu, X.; Bloemsma, E. A.; Steiner, C. P.; Jensen, R. A.; Rebentrost, P.; Eisele, H.; Tokmakoff, A.; Lloyd, S.; Nelson, K. A.; Nicastro, D.; Knoester, J.; Bawendi, M. G. Robust Excitons Inhabit Soft Supramolecular Nanotubes. *Proc. Natl. Acad. Sci. U. S. A.* **2014**, *111*, 3367−75.

(26) Clark, K. A.; Cone, C. W.; Vanden Bout, D. A. Quantifying the Polarization of Exciton Transitions in Double-Walled Nanotubular J-Aggregates. *J. Phys. Chem. C* **2013**, *117*, 26473−26481.

(27) Kasha, M.; Rawls, H.; El-Bayoumi, M. The Exciton Model in Molecular Spectroscopy. *Pure Appl. Chem.* **1965**, *11*, 371−392.

(28) Brixner, T.; Mančal, T.; Stiopkin, I. V.; Fleming, G. R. Phase-Stabilized Two-Dimensional Electronic Spectroscopy. *J. Chem. Phys.* **2004**, *121*, 4221−4236.

(29) Olivero, J. J.; Longbothum, R. L. Empirical Fits to the Voigt Line Width: A Brief Review. *J. Quant. Spectrosc. Radiat. Transfer* **1977**, *17*, 233−236.

(30) Pugžlys, A.; Augulis, R.; Van Loosdrecht, P. H. M.; Didraga, C.; Malyshev, V. A.; Knoester, J. Temperature-Dependent Relaxation of Excitons in Tubular Molecular Aggregates: Fluorescence Decay and Stokes Shift. *J. Phys. Chem. B* **2006**, *110*, 20268−20276.

(31) Stewart, J. J. P. Optimization of Parameters for Semiempirical Methods V: Modification of NDDO Approximations and Application to 70 Elements. *J. Mol. Model.* **2007**, *13*, 1173−1213.

(32) Frisch, M. J.; Trucks, G. W.; Schlegel, H. B.; Scuseria, G. E.; Robb, M. A.; Cheeseman, J. R.; Scalmani, G.; Barone, V.; Petersson, G. A.; Nakatsuji, H.; Li, X.; Caricato, M.; Marenich, A. V.; Bloino, J.; Janesko, B. G.; Gomperts, R.; Mennucci, B.; Hratchian, H. P.; Ortiz, J. V.; Izmaylov, A. F.; et al.. *Gaussian 09*, Revision D.01; Gaussian Inc., 2009.

(33) Zerner, M. C.; Loew, G. H.; Kirchner, R. F.; Mueller-Westerhoff, U. T. An Intermediate Neglect of Differential Overlap Technique for Spectroscopy of Transition-Metal Complexes. *J. Am. Chem. Soc.* **1980**, *102*, 589−599.

(34) Hestand, N. J.; Spano, F. C. Molecular Aggregate Photophysics beyond the Kasha Model: Novel Design Principles for Organic Materials. *Acc. Chem. Res.* **2017**, *50*, 341−350.

(35) Schreiber, M.; Toyozawa, Y. Numerical Experiments on the Absorption Lineshape of the Exciton under Lattice-Vibrations. {II}. The Average Oscillator Strength per State. *J. Phys. Soc. Jpn.* **1982**, *51*, 1537−1543.

(36) Moix, J. M.; Khasin, M.; Cao, J. Coherent Quantum Transport in Disordered Systems: I. The Influence of Dephasing on the Transport Properties and Absorption Spectra on One-Dimensional Systems. *New J. Phys.* **2013**, *15*, 85010.

(37) Lee, P. A.; Ramakrishnan, T. V. Disordered Electronic Systems. *Rev. Mod. Phys.* **1985**, *57*, 287−337.

(38) Clark, K. A.; Krueger, E. L.; Vanden Bout, D. A. Direct Measurement of Energy Migration in Supramolecular. *J. Phys. Chem. Lett.* **2014**, *5*, 2274−2282.

(39) Stone, K. W.; Gundogdu, K.; Turner, D. B.; Li, X.; Cundiff, S. T.; Nelson, K. A. Two-Quantum 2D FT Electronic GaAs Quantum Wells. *Science* **2009**, *1169*, 1169−1174.

DOI: 10.1021/acsnano.8b00911
ACS Nano XXXX, XXX, XXX−XXX